

Submitted to
 JOURNAL OF PHYSICAL OCEANOGRAPHY
 (in revision, October 2020)

Long-distance radiation of Rossby waves from the equatorial current system

J. THOMAS FARRAR*

Woods Hole Oceanographic Institution, Woods Hole, Massachusetts USA

THEODORE DURLAND

College of Earth, Ocean and Atmospheric Sciences, Oregon State University, Corvallis, Oregon USA

STEVEN R. JAYNE, JAMES F. PRICE

Woods Hole Oceanographic Institution, Woods Hole, Massachusetts USA

ABSTRACT

Sea-surface height (SSH) variability throughout much of the North Pacific is coherent with the SSH signal of the tropical instability waves (TIWs) that result from instabilities of the equatorial currents. This variability has regular phase patterns consistent with barotropic Rossby waves radiating energy away from the unstable equatorial currents, and the waves clearly propagate from the equatorial region to at least 30°N. Numerical simulations further support this interpretation. North of 40°N, more than 6000 km from the unstable equatorial currents, the SSH field remains coherent with the near-equatorial SSH variability, but it is not as clear whether the variability at the higher latitudes is a simple result of barotropic wave radiation from the tropical instability waves. Even more distant regions, as far north as the Aleutian Islands off of Alaska and the Kamchatka Peninsula of eastern Russia, have SSH variability that is significantly coherent with the near-equatorial instabilities. The variability is not well represented in a widely used gridded SSH data product, and this appears to be a result of the assumed form of the autocovariance function used for the objective mapping scheme. The pattern of SSH variance at TIW frequencies exhibits remarkable patchiness on scales of hundreds of kilometers, which we interpret as being due to topographic refraction and trapping.

1. Introduction

The major ocean currents are accelerated and maintained by momentum input from the large-scale wind field. The currents strengthen to the point that they become unstable and begin to meander, as energy is transferred to oscillatory instabilities that fundamentally alter the energy and momentum balances of the currents. The instabilities that form may be trapped in the vicinity of the current, or they may instead develop as wavelike disturbances that can radiate energy and momentum to distant locations. Waves radiated from unstable currents can transmit energy and momentum efficiently over long distances and then transfer it to other motions (like the mean flow).

The basic mechanism for radiation of waves from an unstable current has been studied extensively in a variety of fluid-mechanical contexts; in the simplest terms, it can be understood as a resonant excitation of propagating waves in the relatively quiescent fluid adjacent to the unstable jet. This can occur when the wavelength and frequency

of the instability match the wavelength and frequency of a free wave mode in the adjacent fluid (e.g., McIntyre and Weissman 1978; Talley 1983b), but it can also occur under less restrictive conditions, like when the instabilities are transient or spatially limited (Hogg 1988) or when the radiation results from nonlinear interactions (Sutherland et al. 1988).

There is ample evidence that variability radiate away from the major unstable current systems to affect variability at distances of up to 1000 km, but the spatial extent of this influence, and the factors determining that extent, have been difficult to assess (e.g., Bower and Hogg 1992; Miller et al. 2007). The reason for this difficulty is essentially that the observational evidence is mostly based on statistical inferences and data records that are limited in space and time, making it difficult to directly observe the wave propagation. For example, statistics of floats and moored current meter data (velocity variances and covariances) have been interpreted as evidence that deep (~1000 m) eddy kinetic energy at distances of several hundred kilometers from unstable currents such as the Gulf Stream can be explained by barotropic Rossby waves radiating from the unstable, meandering currents (Hogg 1988;

* *Corresponding author address:* Department of Physical Oceanography, Woods Hole Oceanographic Institution, Mail Stop 29, Woods Hole, Massachusetts USA.
 E-mail: jfarrar@whoi.edu

Bower and Hogg 1992; Spall 1992; Waterman et al. 2011). The results have not been completely unambiguous, as the statistics show marked variability on short spatial scales, possibly a result of complex effects of topographic refraction (Bower and Hogg, 1992). Nonetheless, radiation of Rossby waves from the unstable Gulf Stream and Kuroshio extensions is believed to be responsible for the Gulf Stream and Kuroshio recirculation gyres that exist to the north and south of the regions where the jets flow eastward into the open ocean (e.g., Jayne et al. 1996; Mizuta 2009; Waterman and Jayne 2011; Waterman et al. 2011). Realistic general circulation model simulations show clear signs of 20-50-day barotropic waves emanating from the Gulf Stream, even at distances of 1000 km or more, but topographic effects complicate the wave properties considerably (Miller et al. 2007).

Farrar (2011) presented an easily visualized example of radiating instabilities in the satellite altimetry record. Tropical instability waves (TIWs) in the Pacific, which form in the east-central equatorial Pacific as a result of instability of the swift equatorial current system, are accompanied by coherent sea-level variations that extend into the subtropics with the wave crests aligned in the northwest-southeast direction (Figure 1, reproduced from Farrar 2011; Holmes and Thomas 2016). These waves have phase propagation and dispersion consistent with an interpretation as barotropic Rossby waves (Farrar 2011). Figure 1 illustrates the phenomenon with a 'snapshot' of the SSH field after bandpass filtering to pass westward-propagating variability having wavelengths of 10° - 25° of longitude and periods of 29-37 days. Although the main TIW SSH signal exceeds 10 cm near 5° N, the color scale is saturated at ± 1.5 cm to emphasize the radiating variability. The color-saturated, wavelike signal seen on 10° S- 10° N in the eastern-central Pacific is the SSH expression of the baroclinic TIWs; the wavelength, period, and cross-equatorial SSH structure of these unstable modes bears a close resemblance to the predictions of a linear stability analysis (Farrar, 2008, 2011).

The wavelike signal seen north of the equatorial waveguide (near 10° - 20° N, 110° - 150° W) is phase locked to and coherent with the main TIW signal, and the space and time scales of this motion obey the dispersion relation of barotropic Rossby waves over a broad range of wavenumber-frequency space. By substituting the zonal wavenumber and frequency of the main TIW signal into the barotropic Rossby wave dispersion relation, one can make a prediction for the meridional wavenumber and the expected orientation of wave crests in latitude and longitude (Farrar 2011); this prediction agrees well with the observed orientation of the wave crests (black line in Figure 1). Because the properties of this off-equatorial wave seem well-described by the dispersion relation of barotropic Rossby waves, it seems reasonable to use that

dispersion relation to estimate the group velocity; the estimated group velocity is nearly due northward at about 50 cm/s (red arrow in Figure 1). Similar variability, also consistent with an interpretation as barotropic Rossby waves, has been seen in modeling studies (Cox 1980; Song and Zlotnicki 2004; Holmes and Thomas 2016). In a simulation of tropical instability waves in the Pacific, Holmes and Thomas (2016) inferred that a substantial fraction ($>10\%$ or about 3 GW) of the total energy lost by the equatorial current system to instability was carried away horizontally by these barotropic Rossby waves.

In the filtered SSH fields examined by Farrar (2011), the waves mostly disappear by the time they reach 20° N. Perplexingly, the same waves seen in the modelling study of Holmes and Thomas (2016) do not weaken at all before reaching 20° N. This paper and its companion (Durand and Farrar submitted) seek to address the questions: What happens to these waves? Why do they disappear? Answering these questions is an essential first step toward understanding the possible nonlocal effects of instabilities such as these on the mesoscale eddy field and the ocean general circulation, because these effects will be a consequence of how and where the waves disappear.

There are a number of plausible explanations for the apparent decay of the waves seen in Figure 1. Farrar (2011) speculated that the decay of the waves as they reach 20° N might be a result of bottom friction. It is also possible that refraction of the waves by the topographic β -effect causes the wavelength of the waves to change so much that they are no longer present within the passband of the filtered SSH field (10° - 25° zonal wavelengths), or that nonlinear interactions cause the wave energy to be transferred to other wavelengths or frequencies. Another possibility is that the waves are distorted somehow in the altimetry data product used by Farrar (2011)—the DUACS¹ gridded SSH product (Pujol et al. 2016) that Farrar (2011) used is produced with a mapping algorithm that has a strong latitudinal variation in its filtering properties. (As we shall see, this turns out to be the main reason why the waves seem to disappear as they travel northward.)

In this paper, we adopt an analysis approach that allows us to track the waves even as their wavelength changes under refraction due to variations in the topographic and planetary β -effects, and we find that SSH variability at 30-day periods is coherent with the TIW SSH signal at distances of thousands of kilometers. We produce a special-purpose gridded SSH product that has spatially uniform filtering properties, and show that spatial variations of the temporal filtering in the DUACS product causes substantial attenuation and distortion of the 30-day waves. Using

¹DUACS stands for Data Unification and Altimeter Combination System (Pujol et al. 2016), and this merged altimetry product is also often referred to as the "AVISO product". (AVISO stands for Archive, Validation, Interpretation des données des Satellite Océanographiques.)

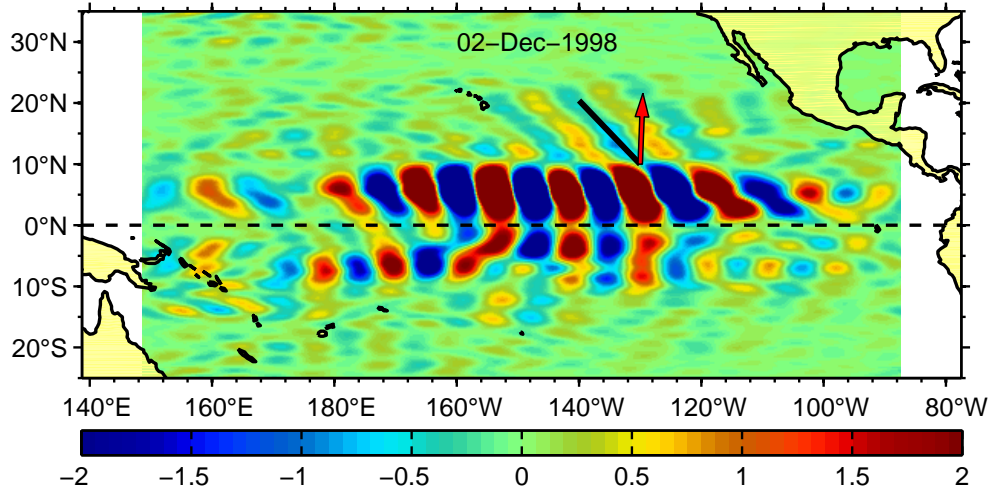


FIG. 1. Filtered SSH fields on 2 Dec 1998, after filtering to pass westward-propagating variability having wavelengths of 10° – 25° of longitude and periods of 29–37 days, with the thick black line indicating the orientation of wave crests expected from the barotropic Rossby wave dispersion relation and the red arrow indicating the expected direction of group velocity. The crest orientation and group velocity direction were computed for an 11.5° zonal wavelength and a 31.5-day period. The barotropic Rossby wave dispersion relation seems to do a good job predicting the orientation of wave crests on 10° – 20° N, 120° – 150° W. Modified from Fig 7a of Farrar (2011).

ray tracing and a barotropic numerical model, we interpret the observed variability as being a result of freely-propagating barotropic Rossby waves that radiate away from their near-equatorial generation region with little influence from atmospheric forcing during their propagation. However, the model does not reproduce some aspects of the coherent variability, and it remains a possibility that there is wind variability at the higher latitudes that is coherent with both the local SSH and the TIWs near the equator.

The paper is organized as follows. Section 2 discusses the data and methods, including the approach used for data gridding, spectral analysis, theoretical ray tracing, and the barotropic numerical model. Section 3 presents the main results of the data analysis, showing the observed long-range coherence of SSH variations with the TIW signal. Section 4 presents an interpretation of the results using a barotropic numerical model and examines how the results are distorted in the widely used DUACS gridded altimetry product. A companion paper (Durland and Farrar submitted) goes into more detail on the theory and modeling of the wave dynamics.

2. Theory, Data and Methods

This section discusses the rationale for the analysis methods and provides a high-level summary of how those methods were implemented. Technical details that may be of interest to some readers are given in appendices.

a. Data

The primary data used for the analysis are sea surface height anomalies from the multi-mission, geophysically corrected, cross-calibrated, unfiltered along-track altimetry data produced and distributed by the Copernicus Marine and Environment Monitoring Service (CMEMS) (<http://www.marine.copernicus.eu>). (These are the same along-track data that were previously distributed by AVISO.) The data were downloaded in January 2016, and the generation of the along-track data product is described in a technical document (AVISO/CLS 2015) and in Pujol et al. (2016). We used all available altimetry data from 1992–2015 (AVISO/CLS 2015; Pujol et al. 2016), which includes data from the following satellite missions: TOPEX/Poseidon, HY-2A, Saral/AltiKa, Cryosat-2, Jason-2, Jason-1, GFO, Envisat, ERS-1, and ERS-2.

b. Gridding of along-track data

We used the along-track altimetry data to produce a gridded SSH product intended to have temporal filtering properties that are roughly uniform in space. (The irregular time-space sampling by the various satellite altimeters makes it impossible to have truly uniform filtering properties in time or space; e.g., Wunsch, 1989; Chelton and Schlax, 1994; Schlax et al., 2001.) We mapped the data to a uniform space-time grid ($0.5^{\circ} \times 0.5^{\circ} \times 3$ days) using a Gaussian weighted-average smoother having nominal half-power points of $6^{\circ} \times 6^{\circ} \times 17$ days. More details are given in Appendix A. For subsequent analysis, we further smoothed the gridded SSH field with a Gaussian filter

having a half-amplitude wavelength of 2° in latitude and longitude. We used the gridded data from 1 January 1993 to 18 April 2015. The total record length used for analysis was 8142 days (>22 years).

There is a readily available and widely used gridded altimetry product known as the “AVISO” or “DUACS” product (AVISO/CLS 2015; Pujol et al. 2016). We initially conducted our analysis with that product, but after trying and failing to make a sensible physical interpretation of the results, we arrived at the conclusion that the spatial variations of 30-day variability in that product must be very strongly affected by spatial variations in the mapping parameters (Appendix B).

c. Theoretical background: Idealization as freely-propagating barotropic Rossby waves

The primary goals of this analysis are to isolate the basin-wide variability in SSH that is associated with TIWs, and to understand how this variability is associated with the waves that have already been observed radiating north from the TIW generation region (Farrar 2011). We will interpret the variability as freely-propagating topographically-modified barotropic Rossby waves, while recognizing that this is an idealization. The combination of stratification and topography, for instance, can modify both the dispersion relation and the vertical structure of topographic waves (e.g., Rhines 1970), to the point where they might no longer resemble our familiar notions of topographic Rossby waves in an unstratified fluid. On the scale of the waves identified by Farrar (2011), the general topographic slopes of the North Pacific are small enough that the SSH signal and propagation characteristics are likely to be altered only moderately, rather than drastically (Durland and Farrar submitted). However, these effects must be kept in mind; in the vicinity of isolated seamounts, fracture zones, and the steep slope on the northern boundary (arising out of the Aleutian trench), the idealization may be particularly bad. Recent work shows that realistic vertical shear of mean currents, even a surface current of only a few cm/s, can appreciably affect the vertical structure of the barotropic mode (Brink and Pedlosky 2020), but this effect should be small for the wavelengths that we consider here. Throughout this paper, our use of “barotropic” is not meant to imply strict depth independence, but rather is a shorthand for a lowest vertical mode signal that most closely resembles the idealized barotropic mode.

With the above caveats in mind, and with the success of Farrar (2011) in interpreting the signals south of 20°N as barotropic Rossby waves, we proceed to interpret the basin-wide SSH signal that is coherent with TIWs as barotropic, topographic Rossby-waves. The phase speed and group velocity inferred by Farrar (2011) (~ 0.5 m/s) are large compared to the inferred particle velocities and

the general current speeds of the North Pacific. A linear interpretation of the waves is thus appropriate. Assuming that the waves are not affected by the time-dependent oceanic motions, their frequency can be expected to remain constant, and a coherence analysis at the dominant TIW frequency should identify the SSH signal of the propagating waves.

d. Theoretical background: ray tracing

Ray tracing is often the first approach used for understanding wave propagation away from a generation region. The technique assumes that changes in the propagation medium are “gradual” (i.e., on length scales much longer than a wavelength). Unfortunately, the bathymetric smoothing required to satisfy this condition attenuates many of the features characteristic of the North Pacific, such as isolated seamounts, the series of fracture zones in the eastern part of the basin, and the steep slopes south of the Alaskan Peninsula and the Aleutian Islands. Accordingly, we minimize our dependence on ray tracing, but we will briefly examine a ray-tracing solution for hints of how the large-scale bathymetric features might influence the Rossby wave propagation.

We solved the ray tracing equations in spherical coordinates following Longuet-Higgins (1965). We used topography from ETOPO 2 (version 2) smoothed with a two dimensional Gaussian smoother that has a half-amplitude wavelength of 33° . The wave rays were initialized along 10°N with a frequency of 33.5 days and a zonal wavelength of $\lambda_x = 16^\circ$ of longitude. The zonal wavenumber is negative so that the waves propagate westward. These values were chosen to be consistent with the values diagnosed in Section 3, based on analysis of more than 20 years of altimetry data. They differ slightly from the values reported in Fig. 1, because Fig. 1 shows a snapshot in time, and the dominant TIW frequency and zonal wavelength vary from year to year, and even within a single year. The initial meridional wavelength depends (through the dispersion relation) on the local topography, but is roughly $\lambda_y = 12^\circ$ of latitude, with a negative meridional wavenumber for poleward energy propagation away from the TIWs. The net wavelength is about 10° degrees, consistent with the observations of Farrar (2011). With the above smoothing and initial wavenumber, the short Rossby wave dispersion relation is appropriate (Durland and Farrar 2020):

$$\sigma = \frac{\hat{e}_z \cdot (\vec{\beta} \times \vec{K})}{|\vec{K}|^2}. \quad (1)$$

The positive radian frequency is σ , \hat{e}_z is the unit vertical vector and \vec{K} is the wavenumber vector. The $\vec{\beta}$ vector is defined as

$$\vec{\beta} \equiv H\nabla(f/H). \quad (2)$$

where f is the Coriolis parameter, $H(\lambda, \theta)$ is the water depth, and λ and θ are the longitude and latitude. The

β vector plays the same dynamical role as ∇f in a flat-bottom solution. As the ray equations were integrated forward in time, we monitored the evolving wavenumbers to ensure the continued validity of the short Rossby wave approximation.

Figure 2 displays ray solutions for North Pacific bathymetry. The wide, magenta vector emanating from 130°W , 10°N in Fig. 2 shows the initial group velocity (parallel to the ray trajectories at 10°N), oriented toward the north-northwest. The red vector shows the direction of phase propagation. The regular phase patterns and parallel ray trajectories south of 20°N are consistent with the observations of Farrar (2011). North of 20°N , the large-scale bathymetry begins to refract the rays toward a more westward direction, causing a convergence of rays in the midlatitudes between 130°W and 150°W . Because the ray tracing is only a preliminary investigation, we do not calculate energy density, or treat the solutions near the caustics. The densely packed ray paths northwest of the strong convergence near 150°W , 43°N are therefore not dependable. Likewise, the gradual westward refraction of the several rays closest to the North American continent should not be relied upon because the topographic smoothing has fundamentally changed the character of the wall-like bottom topography at the northern boundary, making it more like a gentle slope. Nevertheless, the calculations suggest that poleward of 20°N we might expect a convergence of wave energy. They also suggest that the influence of the equatorially generated waves might be felt in the far northwestern corner of the basin. This is probably the limit of what we might deduce from the simple ray tracing approach.

e. Spectral analysis methods and approach

With the expectation that the frequency of the waves will remain constant but that their wavenumber may change as they encounter variations in water depth and the β -effect, we chose to carry out our data analysis in the frequency-latitude-longitude domain in order to focus on the 33-day period band without constraining the wavenumber (in contrast to the wavenumber-frequency analysis of Farrar, 2011). We did this by estimating cross-spectral quantities, like squared coherence, gain, and phase between the SSH time series at 5°N , 130°W (where the 33-day TIW variability is strongest) and all other locations. The resulting map of squared coherence allows us to identify locations where the SSH variability is coherent with the 33-day TIW variability, the map of gain allows us to estimate the pattern of the amplitude of the coherent SSH variability, and the map of phase allows us to quantify the spatial variations of the phase of the SSH signal that is related to the TIWs. Like the ray tracing, this approach exploits our expectation that the wave frequency will be

preserved as the waves propagate away from their forcing region, but, unlike the ray tracing, there is no implicit assumption that the wave propagation must change only gradually. Another difference from the ray tracing analysis is that a broad range of zonal and meridional wavenumbers may contribute to the variability in a given frequency band—the analysis places no constraint on the wavenumber, except for the fact that short wavelengths ($< \sim 6^\circ$) are suppressed by the mapping of the SSH data.

To estimate the frequency power spectral density (“spectrum”) of SSH and the cross-spectrum of SSH between pairs of locations, we first removed the time mean of the SSH anomaly at each location and applied a taper window (a Tukey, or tapered cosine, window) that brings the time series smoothly to zero over the first and last 10% of the time series (Harris 1978). We then computed the Fourier coefficients (using MATLAB’s fast Fourier transform):

$$\hat{h}(\omega) = \sum_{n=-N/2}^{N/2-1} h_n e^{-2\pi i \omega t_n} \quad (3)$$

where h_n is the value of SSH at a given location at time n , N is the total number of data points at that location, $\omega = m/(N\Delta t)$ is the dimensional frequency (not radian), and $t_n = n\Delta t$. (If N is odd, as it actually is in our analysis, the summation is over $-(N-1)/2$ to $(N-1)/2$.) In our analysis, the fundamental frequency resolution is $1/(N\Delta t) = 1/(8145 \text{ days})$.

The one-sided power spectral density (Bendat and Piercol 2010, p.399-400) at each point expresses the variance of h within a given frequency band:

$$\Psi_h(\omega, \lambda, \theta) = \left\langle \frac{2\Delta t}{N} \hat{h}^* \hat{h} \right\rangle \quad (4)$$

where the asterisk indicates the complex conjugate and the angle brackets indicate the expectation value (which we will approximate by averaging over 13 adjacent frequency bands).

The Fourier coefficient $\hat{h}(\omega, \lambda, \theta)$ expresses the amplitude and phase of SSH at the frequency ω at the longitude λ and latitude θ . If there is wave radiation from a source region that affects the SSH at the location (λ, θ) via linear wave dynamics, we would expect part of the SSH signal $\hat{h}(\omega, \lambda, \theta)$ to be linearly related to (i.e., to have a fixed amplitude and phase relationship to) the SSH in the source region. Of course, there may also be contributions to the SSH signal $\hat{h}(\omega, \lambda, \theta)$ that are completely unrelated to the SSH signal in the source region. We can express this situation as,

$$\hat{h} = \alpha_n \hat{h}_0 + \hat{n}, \quad (5)$$

where $\hat{h}_0(\omega, \lambda_0, \theta_0)$ is the SSH at a reference location in the hypothesized source region, the “transfer function” $\alpha_n(\omega, \lambda, \theta)$ is a complex number that relates the amplitude and phase of the SSH at the reference location to that

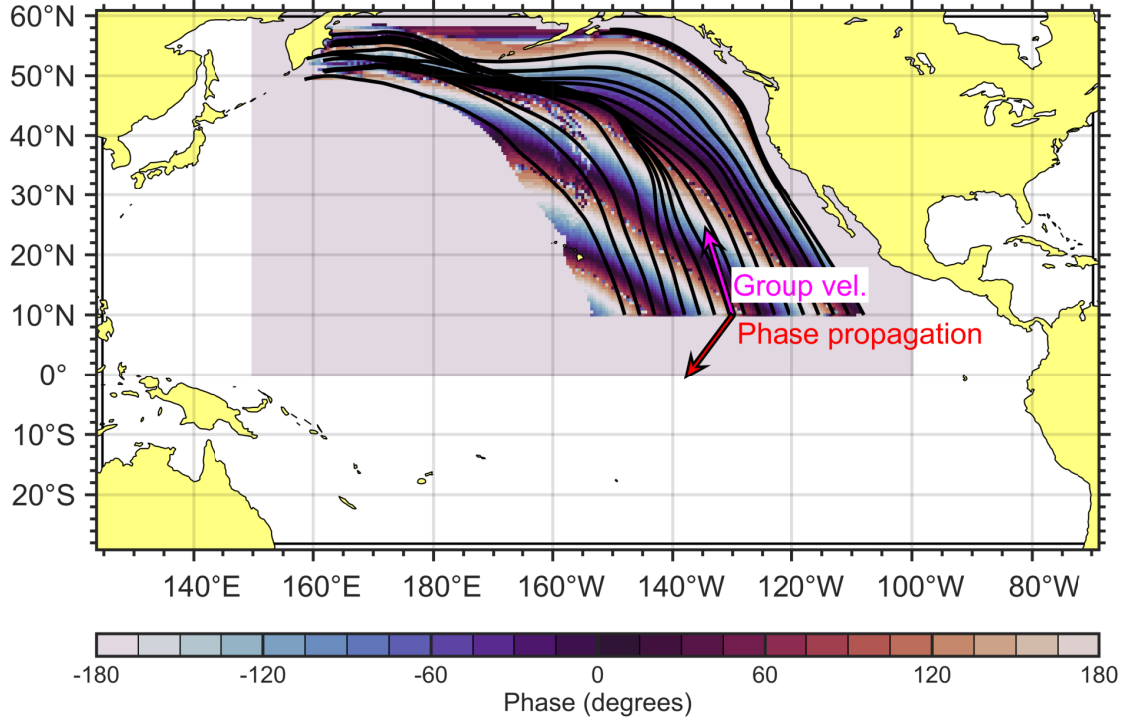


FIG. 2. Ray paths for a wave leaving 10°N with 33.5-day period and 16° zonal wavelength. ETOPO2 North Pacific bathymetry has been smoothed with a two dimensional Gaussian smoother having a half-amplitude wavelength of 28° . Black lines indicate the paths of energy propagation, as the waves are refracted by variations in the ocean depth and the Coriolis parameter. The color shading indicates the wave phase, and the red vector shows the direction of phase propagation. The magenta arrow indicates the initial group velocity vector of the wave.

at the position (λ, θ) , and $\hat{n}(\omega, \lambda, \theta)$ is the contribution to the SSH signal that is not related to \hat{h}_0 (i.e., that is linearly independent of \hat{h}_0).

We can solve for the transfer function α_h by first multiplying both sides of Equation 5 by \hat{h}_0^* and then taking the expectation value:

$$\langle \hat{h}_0^* \hat{h} \rangle = \alpha_h \langle \hat{h}_0^2 \rangle + \langle \hat{h}_0^* \hat{n} \rangle, \quad (6)$$

where we are using the shorthand notation $\hat{h}_0^2 = \hat{h}_0^* \hat{h}_0$. We have defined \hat{n} as being independent of \hat{h}_0 , so $\langle \hat{h}_0^* \hat{n} \rangle = 0$. Thus,

$$\alpha_h = \frac{\langle \hat{h}_0^* \hat{h} \rangle}{\langle \hat{h}_0^2 \rangle}. \quad (7)$$

The transfer function, $\alpha_h(\omega, x, y)$, is complex, and it is useful to write it as a magnitude and phase:

$$\alpha_h = |\alpha_h| e^{i\phi} \quad (8)$$

The magnitude of the transfer function $|\alpha_h|$ is referred to as the “gain”, and its phase ϕ expresses the phase shift between h and h_0 at the frequency ω . The phase of the transfer function is identical to the phase of the cross-spectrum of h and h_0 , so we will refer to ϕ as the cross-spectral phase.

We can determine the portion of the variance of the SSH at the location (λ, θ) and frequency ω that is linearly related to the SSH at the reference location by squaring Equation 5, taking the expectation value and again using the fact that $\langle \hat{h}_0^* \hat{n} \rangle = 0$, to obtain,

$$\langle \hat{h}^2 \rangle = \alpha_h^2 \langle \hat{h}_0^2 \rangle + \langle \hat{n}^2 \rangle. \quad (9)$$

Multiplying both sides by the spectral normalization constant $2\Delta t/N$ allows us to write this in terms of the total variance of each term within the frequency band (i.e., in terms of spectral density):

$$\Psi_h = \alpha_h^2 \Psi_{h_0} + \Psi_n \quad (10)$$

The quantity $\alpha_h^2 \Psi_{h_0}$ is the portion of the variance of the SSH at the location (λ, θ) and frequency ω that is linearly related to the SSH signal at the reference location. Dividing that quantity by Ψ_h , the total variance of SSH in the frequency band at that location, gives the fraction of the variance of h that is linearly related to the signal \hat{h}_0 ,

$$\gamma_h^2 = \frac{\alpha_h^2 \Psi_{h_0}}{\Psi_h} = \frac{\langle \hat{h}_0^* \hat{h} \rangle^2}{\langle \hat{h}^2 \rangle \langle \hat{h}_0^2 \rangle}, \quad (11)$$

which is also known as the squared coherence amplitude.

We estimated the gain and phase of the transfer function (Eqn. 8) and the coherence squared (Eqn. 11) between each point and the reference location (5.125°N , 130.0°W , which we will refer to hereafter as 5°N , 130°W). We chose this reference location because it is the place where the 33-day SSH variance is strongest (Section 3). We averaged over 13 adjacent frequency bands (frequencies spanning 0.0290–0.0306 cpd or periods of 32.65–34.44 days) in order to increase the number of degrees of freedom of the estimate, and we reduced the estimated number of degrees of freedom to account for the use of a taper window as described below. The center of the frequency band has a period of 33.52 days, and the frequency band is hereafter referred to as the “33-day period band”.

Application of a taper window to a time series introduces a linear dependency among adjacent Fourier frequency bands and makes frequency-band averaging less effective at increasing the number of degrees of freedom of the spectral estimate. Following Bloomfield (2000, p. 184), we accounted for the reduction of the number of degrees of freedom of the spectral analysis and coherence amplitude caused by the tapering; this approach suggests the effective number of degrees of freedom should be reduced by 10.5% relative to the number of degrees of freedom that would be expected with no tapering. We used this reduced number of degrees of freedom in the formula given by (Thompson 1979) to estimate the coherence significance level at 95% confidence. We tested the validity of this approach using Monte Carlo simulations of the coherence for random time series having red spectra and found it to be quite accurate.

Our choice of reference location for the cross-spectral calculations is not entirely arbitrary (being the site where the TIW SSH signal is strongest), but the reader may wonder whether our results are sensitive to this choice. They are not—we present some representative results using other reference locations in Appendix C. We also performed an analysis similar to the cross-spectral one used here but with frequency-domain empirical orthogonal functions (e.g., Mizuta 2009), a technique that does not require use of a reference location at all—the resulting patterns of amplitude and phase were nearly identical to the ones shown here and will not be discussed. (We prefer the cross-spectral analysis because it is simpler.)

3. Observed 33-day SSH variability

The SSH field in the equatorial Pacific exhibits strong variability at periods of about 33 days (e.g., Lee et al. 2018; Farrar 2008, 2011; Lyman et al. 2005). We can quantitatively assess the spatial pattern of this 33-day variability by estimating the frequency spectral density of SSH at each location and displaying a map of the spectral density in the 33-day period band (Figure 3). There is a broad, zonally elongated ridge of high variance near 5°N in the

eastern and central Pacific ($100\text{--}170^{\circ}\text{W}$) associated with the 33-day TIW activity, and there is another, weaker ridge near 5°S associated with the southern hemisphere expression of the TIWs.

The SSH variability is strongest near $5\text{--}6^{\circ}\text{N}$, 130°W (Figure 3), and the existence of this local maximum in 33-day SSH variance is clearly due to the TIWs. We will thus use 5°N , 130°W as a “reference location”, and we will sometimes refer to the 33-day SSH variability at this location as the “33-day TIW signal”. The 33-day variability is also strong in the Kuroshio Extension region, but as we will see, this variability is not coherent with the TIWs.

A remarkable feature of the map of the spectral density in the 33-day period band (Figure 3) is that it is extremely patchy, with order-of-magnitude changes in variance over distances on the order of 1000 km (10°). This is not only true when comparing the unstable current jets (equatorial currents and Kuroshio) to the mid-ocean gyres—it is also true when comparing the SSH variance in one open-ocean region to another. This patchiness does not appear to be a mere result of noise or lack of stability in the spectral calculation (differences in variance of 6 contour levels exceed the estimated 95% confidence interval, and this corresponds to about a factor of four in variance). For example, there is about a factor of 20 change in variance between the local minimum of variance near the Baja Peninsula (western Mexico) and the relative maximum 1500 km to the southwest near 20° , 140°W , and there is a factor of 5 change in variance between the local minimum near 10.5°N , 140°W and the location 390 km due north of there (near 14°N , 140°W)—these differences exceed the 99% confidence interval. Below and in a companion paper, we argue that this patchiness is a dynamical consequence and topographic refraction of the radiating waves.

In an attempt to isolate the SSH variability at 33-day periods that is associated with the TIW variability, we estimated the coherence between the SSH time series at 5°N , 130°W (the reference location) and the SSH at all other locations (Figure 4). Throughout a large region of the tropical and North Pacific², the 33-day SSH signal is coherent with that in the TIW region at high levels (squared coherence >0.5) that are different than zero at 95% confidence or better (indicated by a white contour in Figure 4). Hereafter, we will sometimes refer to the squared coherence amplitude as the “coherence”, and we will sometimes omit specific mention of the 33-day period band, though it should be understood that all results apply to this period band (Section 2).

²We only display the results for the tropical and North Pacific because this is where the most robust coherence pattern is detected. Previous work looking for evidence of radiation in the tropics and the immediate vicinity of the TIWs mostly found radiation only to the north (Farrar 2011). We have checked again and could not find clear evidence of radiation farther into the South Pacific. One might imagine this could be because the TIWs are stronger on the northern side of the equator. However, realistic model simulations show clear evidence of southward

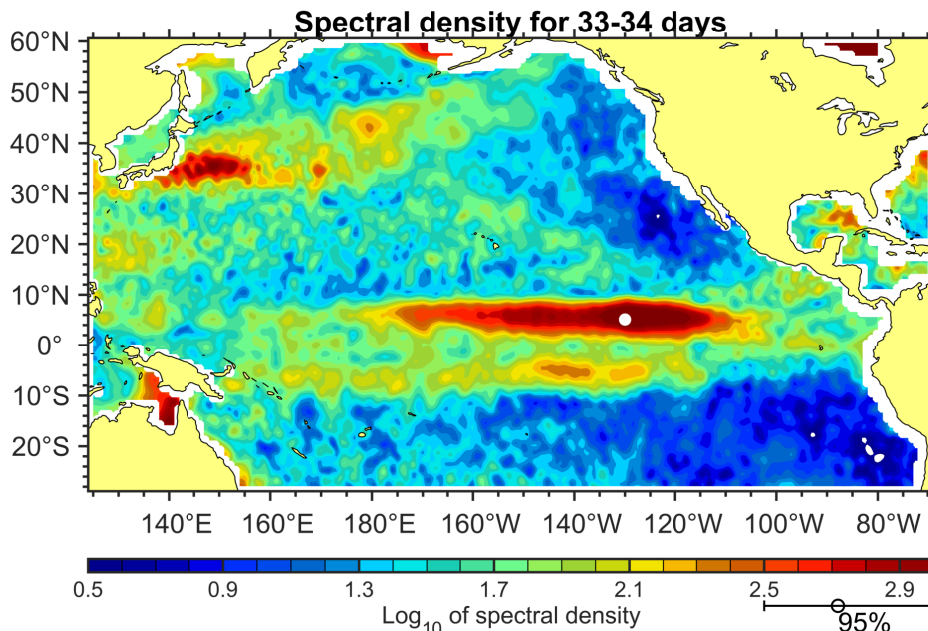


FIG. 3. Base-10 logarithm of spectral density of SSH (cm^2/cpd ; proportional to variance or squared amplitude) in the 33-day period band. The 95% confidence interval for the spectrum is shown on the bottom-right side of the colorbar—spectral differences of about 6 contour levels can be considered statistically significant. The white circle at 5.125°N , 130°W indicates the position used for the reference time series.

There is a region of high coherence in the main TIW region ($\pm 10^\circ$ from the equator), with ridges of high coherence found along 5°N and 5°S where the TIW variability is strong (Figure 4). That the SSH along 5°S is coherent with the 33-day SSH signal at 5°N reflects the expected mode-like structure of the TIWs (Lyman et al. 2005; Farrar 2008, 2011). Remarkably, the coherence between the reference location (5°N , 130°W) and its ‘mirror-image’ location south of the equator (5°S , 130°W) is higher than the coherence between the reference location and locations just one TIW wavelength (about 15° of longitude) to the west.

There are also many locations outside of the immediate TIW region where the SSH variability is significantly coherent with the 33-day TIW SSH signal at the reference location (Figure 4). The spatial pattern of coherence has a patchy character (for which we will later offer a physical interpretation). There are fairly large patches of significant coherence as far south as 20°S and as far north as 50°N , adjacent to the Aleutian Islands off Alaska and the Kamchatka Peninsula in Russia (northeast of Japan). There are also many smaller patches of statistically significant coherence, with radii of a few degrees or less, scattered throughout the Pacific (and even the Atlantic)—we

should not overinterpret these fine details of the coherence map, because we expect the 95% significance level to be exceeded at 5% of the locations as a result of pure chance.

Outside of the immediate TIW region ($\sim 10^\circ\text{N}$ – 10°S), there are several large patches exhibiting significant coherence with the TIW SSH signal. The largest of them spans the 10 – 20°N region and is the same region studied previously by Farrar (2011). Squared coherence amplitudes exceed 0.6 over much of this region, indicating that more than 60% of the variance of SSH at 33-day periods can be predicted from the TIW signal at the reference location. There is another large patch just to the north, near 30°N , 125 – 140°W , and there are two more large patches of significant coherence to the northwest near 40 – 50°N . In all of these patches, the squared coherence amplitude is roughly 0.5 or higher, indicating that half of the SSH variance at 33-day periods can be predicted from the TIW signal³. It is remarkable that the squared coherence amplitude is higher in many of these distant patches than it is only 15 – 20° to the east or west of the reference location. This is somewhat surprising because the TIW propagation is due westward, and so one would expect the coherence to be highest to the west or east of the reference location. One possible reason for the low coherence at locations to the east and west in the TIW region is that the TIW variability contains different wavenumbers at the same frequency

radiation (e.g., Holmes and Thomas 2016), so this needs further investigation. The model simulations of Holmes and Thomas (2016) and Cox (1980) showed southward radiation but did not have realistic topography, which suggests the lack of southward radiation in the observations could be a dynamical consequence of topography.

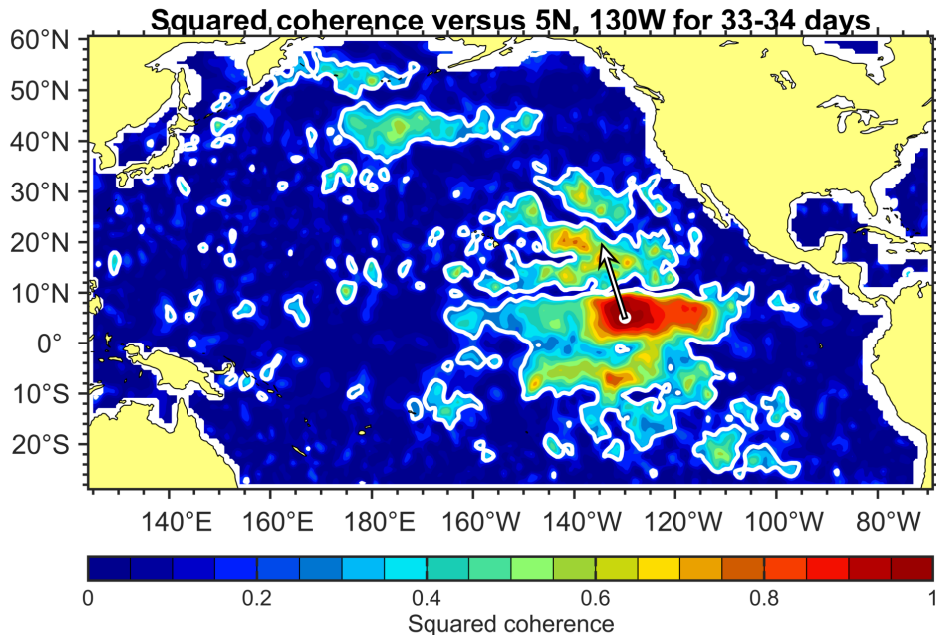


FIG. 4. Squared coherence (dimensionless, ranging from 0 to 1) between SSH in the 33-34 day period band at 5°N, 130°W (white circle) and all other locations. The squared coherence gives the fraction of variance explained at each location (at 33-day periods) by the SSH at the reference location. White contours surrounding regions of high coherence represent the level at which the coherence is different from zero at 95% confidence. The white arrow shows the expected direction of propagation of barotropic Rossby wave energy (assuming a 33-day period and 16° zonal wavelength).

(Farrar 2011), which would be expected to degrade the coherence.

The associated map of phase (Fig. 5) shows the expected patterns of (a) the baroclinic TIWs in the equatorial waveguide ($\sim 10^\circ\text{N}$ - 10°S) with dominantly westward phase propagation and (b) the northwest-to-southeast oriented phase lines associated with northward-radiating barotropic Rossby waves in the region immediately north of the strongest TIW activity (i.e., 10 - 20°N , 115 - 155°W). As in the ray tracing, these phase lines extend northwestward in fairly straight lines to as far as 35°N , where they begin to bend toward a more westward direction. Further poleward, the phase isolines take a more east-west orientation, with a large region of in-phase behavior (i.e., more gradual phase variations) in the northeast Pacific near 45°N and 175°E - 145°W . The reader might notice that the zonal wavelength in the 10 - 20°N region is somewhat longer in Fig. 5 than it is in Fig. 1—Fig. 5 is a composite over the whole record, whereas Fig. 1 represents a partic-

ular time, and there is some year-to-year variability in the dominant wavelength and frequency of the TIWs and the radiated variability.

We can obtain an estimate of the relative amplitude of variability coherent with the TIW SSH signal by estimating the gain relative to the SSH at the reference location. The resulting map of the gain in the 33-day period band (Figure 6) has a pattern that is similar to the map of coherence, with elevated gain in the TIW region, in the 10 - 20°N region to the north of the TIW region, and in a region spreading to the northwest around 40°N . To get a measure of which parts of the gain estimate are most robust, we estimated the relative error of the gain following Bendat and Piersol (2010, p. 309, their Eqn 9.90), and we included a white contour in Figure 6 to indicate the places where the gain error is estimated to be less than 30% of the estimated gain. The pattern of the relative error in the gain closely resembles the pattern of coherence amplitude. There are small patches of high gain in the Kuroshio extension region (around 35°N near Japan) that are of questionable significance—the estimated coherence in this region was insignificant, the relative error in the gain was above 30%, and we suspect the high gain values are the spurious result of high variance coupled with the inevitable bias of coherence estimates near zero.

³The reader may wonder whether the spatial patterns of the squared coherence amplitude, and associated spectral quantities like gain and phase, are sensitive to the choice of reference location. We have examined this sensitivity, choosing reference locations inside and outside the other patches of high coherence. The detailed patterns of coherence, gain, and phase do depend on the choice of reference location, but in a way that is consistent with the hypothesis that barotropic wave propagation is responsible for the observed long-range coherence (Appendix C).

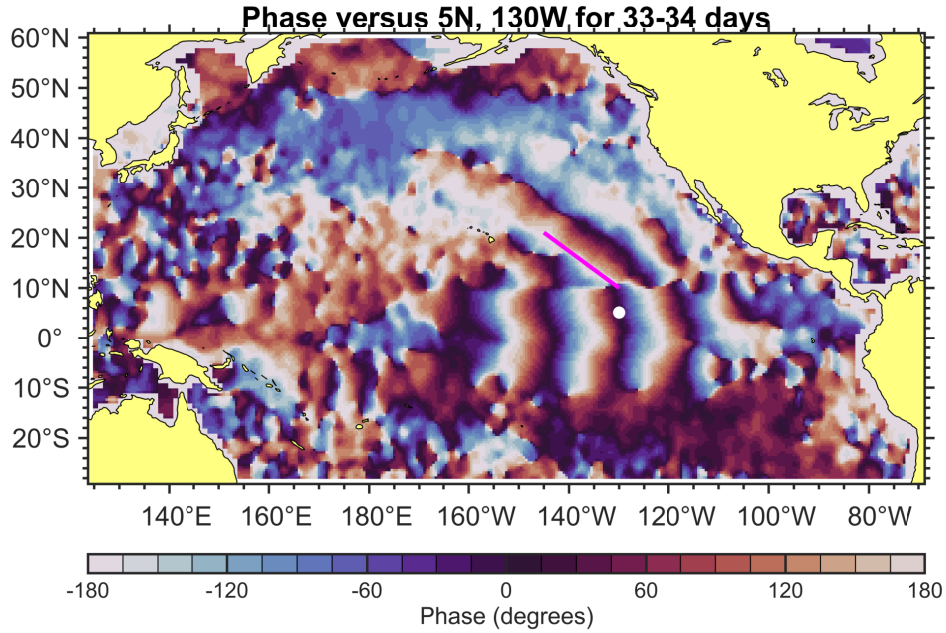


FIG. 5. Coherence phase (degrees) between SSH in the 33-34 day period band at 5°N , 130°W (black circle) and all other locations. The sign convention of phase is such that phase at a fixed geographical position progresses in time from blue to white to red (i.e., from positive values to negative values). The magenta line shows the expected orientation of barotropic Rossby wave crests at 33.5-day periods and the zonal wavelength of the TIWs (estimated to be 16° of longitude).

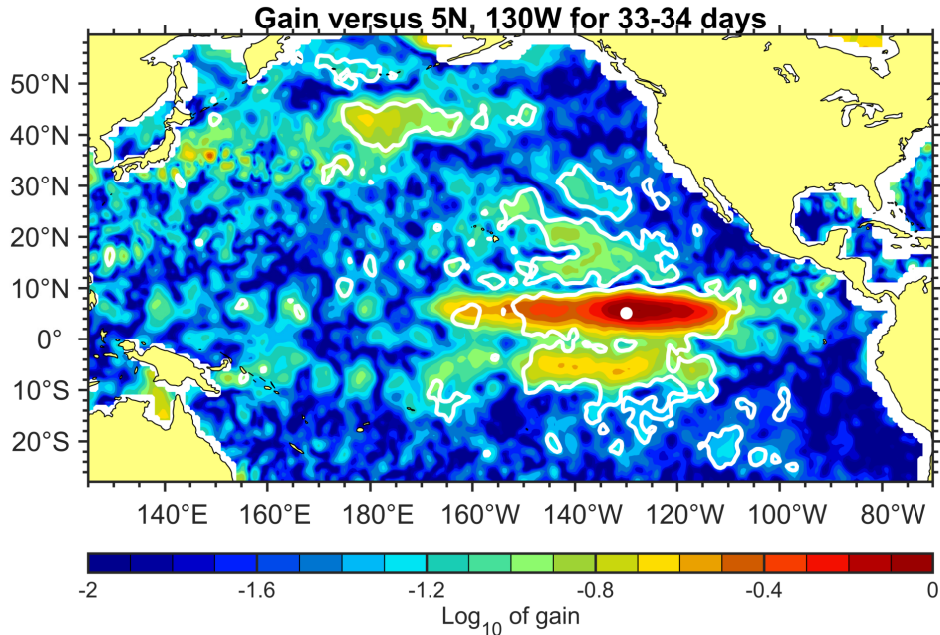


FIG. 6. Base-10 logarithm of gain factor between SSH in the 33-34 day period band at 5°N , 130°W (white circle) and all other locations. Inside the white contours, the relative error in the estimated gain is estimated to be less than 30%.

4. Interpretation and Discussion

There were two important results in the previous section. First, there is SSH variability at distant locations

throughout the North Pacific that is coherent with SSH signal of tropical instability waves. At locations 3000 or

even 6000 kilometers away from the unstable equatorial currents, about half of the SSH variance at 33-day periods can be explained by the TIW SSH signal. Second, these remote, coherent signals exhibit remarkable ‘patchiness’ in their spatial patterns, and this patchiness is reflected in the pattern of variance (spectral density) and the coherence amplitude and gain relative to the place where the TIW signal is largest.

It is clear from prior work that barotropic Rossby waves radiate energy northward from the unstable equatorial currents, which provides a seemingly obvious interpretation of the coherence of remote SSH variability with the TIW SSH signal. However, the patchiness of the coherence, with regions of high coherence separated by regions of low coherence, might cause one to question this interpretation. In addition, one might wonder whether the large patches of coherent variability found at very great distances from the equatorial currents could be explained by the wind or some other atmospheric forcing that is coherent over planetary scales. Below, we examine the radiating wave interpretation in light of the numerical modeling study conducted in a companion paper (Durland and Farrar submitted). We conclude the paper by revisiting the question of why the waves seemed to disappear in the analysis of Farrar (2011).

a. Interpretation of observed 33-day SSH variability in light of model results

A limited theoretical account of the expected behavior of the waves after they leave their generation region was given based on ray tracing (Section 2d). That account is limited for several reasons, including that the outgoing waves included only a single wavenumber and frequency and that application of the ray tracing approach required that we smooth the topography over scales longer than a wavelength. There are some qualitative similarities, and some differences, between the ray-tracing phase estimate and the phase estimate from the observations.

In a companion paper (Durland and Farrar submitted), we made a more thorough theoretical analysis of the problem using a more realistic barotropic numerical model and other tools, and we would like to highlight some of those results for discussion here. Especially relevant to the present discussion is the role of topography in generating the spatial patchiness that is observed in the SSH amplitude.

As described in more detail in the companion paper (Durland and Farrar submitted), we configured a linear, primitive equation barotropic model with realistic bathymetry for a North Pacific domain and forced the model with a ‘wave maker’ along the model domain’s southern boundary at 10°N. The ‘wave maker’ was a fluctuating meridional velocity, with a zonal wavenumber, frequency, and a zonal envelope meant to mimic, in an

idealized way, the properties of TIWs and the outgoing wave packets. The boundary forcing propagates westward at a speed of 0.62 m/s, and has a period of 33.5 days and a dominant wavelength of 16°, with a range of wavenumbers about this value being required so that the forcing packet can be localized in space (Durland and Farrar submitted). The pattern of the forcing is depicted in Fig. 7 (upper panel), which shows the boundary forcing at a particular time. The forcing amplitude was increased gradually from zero and then held steady until the model reached a statistically steady state.

The pattern of the phase of SSH in the model is displayed in Fig. 7, along with the observed phase of SSH variability relative to the TIW reference location. When comparing the modeled phase and the observed phase, attention should be focused on the area north of the forcing; outside of this area, the model SSH has very low amplitude and observed SSH is not really coherent with the TIW forcing. There are qualitative similarities and differences between the observed and modeled phase. Between 10° and 35° N, the phase lines in both the model and the observations are fairly straight and oriented from the southeast to the northwest (Fig. 7). Poleward of 30° – 35° N, the phase lines begin to refract toward a more westerly direction, and the phase patterns become more diffuse and less regular.

The variability at every point in the linear model is perfectly coherent with the idealized TIW forcing, so the model’s stationary-state SSH amplitude is best compared with the observed coherence gain: that part of the observed SSH amplitude that is coherent with the TIW reference SSH. The comparison can be seen in Fig. 8, with the model amplitude shown in the top panel, and selected contours of the model amplitude superimposed on the observed coherence gain in the bottom panel. South of 35°N, the model results compare fairly well with the observations, especially in the broad pattern of elevated amplitude and in the qualitative nature of the highs and lows.

Remarkably, the model amplitude field exhibits the same sort of patchiness that the observed field does. In the model, the patchiness of the amplitude pattern between 10°N and 40°N is due to two effects: wave interference and topographic refraction (Durland and Farrar submitted).

Topographic refraction contributes to the patchiness of the amplitude pattern. As the waves encounter topographic gradients, their energy is refracted and focused, creating spatial variations in SSH amplitude. The model experiments with and without variable bottom topography suggest that topographic refraction is the reason for the patchiness on smaller scales. An additional consequence of the topographic refraction seen in the model experiments is that the refraction and trapping of wave energy by the topography effectively lengthens the path length for

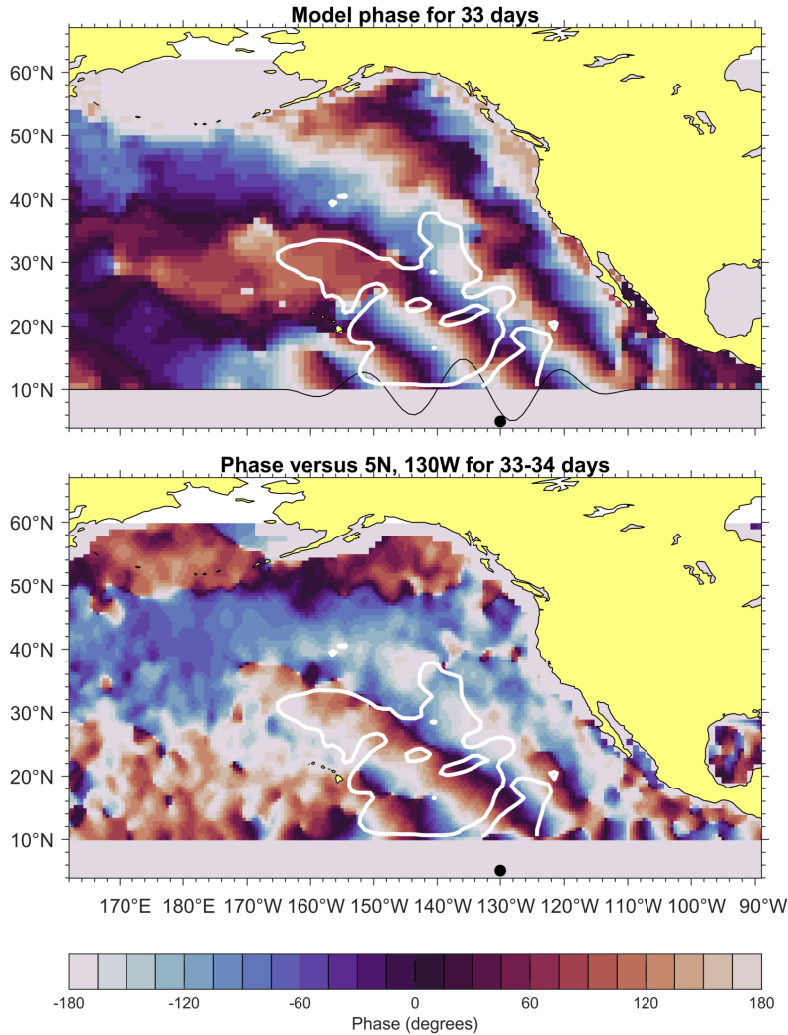


FIG. 7. Top panel: Phase of modeled 33-day SSH signal. Bottom panel: Observed phase relative to the 33-day SSH signal at 5°N , 130°W (location indicated by a black dot). In the top panel, the meridional velocity used to force the model at 10°N is depicted by a black line; this modulated sinusoid propagates westward at the TIW phase speed.

the wave energy (e.g., as wave energy flux vectors circulate around sea mounts), causing the wave energy to decay more rapidly with distance from the source than it would in the absence of topography (Durland and Farrar submitted). (See Durland and Farrar submitted, for a more extensive discussion of these model experiments, the pattern of energy fluxes, and the temporal evolution after the onset of the forcing.)

The qualitative agreement between the modeled and observed amplitude patterns is reasonably good south of about 35°N , but there is a conspicuous disagreement near 44°N , 180°E , where the observations show a ‘hot spot’ of locally elevated amplitude. The model also exhibits a local maximum at this location, but the relative amplitude is about five times smaller than in the observations. We offer more discussion of this discrepancy below.

Despite the discrepancy near 44°N , 180°E , the model results do show that it is reasonable to interpret most of the observed coherent SSH variability as being due to the barotropic waves radiated from tropical instability waves, especially within about 3000 km of the instabilities. The more distant feature near 44°N , 180°E is unquestionably coherent with the SSH signal in the TIW region—about half of the variance of SSH at 33-day periods at 44°N , 180°E can be predicted from the time series of SSH in the TIW region—but replaced because since we cannot reproduce the feature in a model or clearly understand how it could be generated by the radiating waves, we cannot confidently ascribe the feature at 44°N , 180°E to the radiating waves.

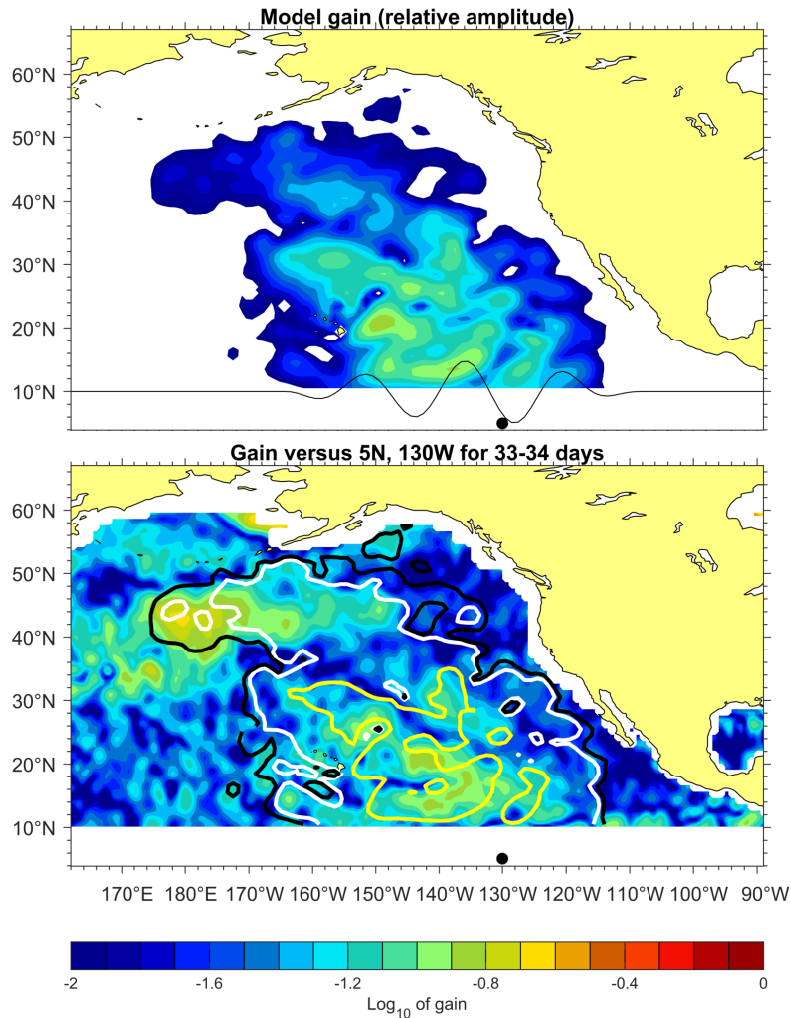


FIG. 8. Top panel: Log_{10} of model SSH amplitude. Bottom panel: Log_{10} of observed gain (or amplitude of coherent variability) relative to 5°N, 130°W (black circle), with contours of model SSH amplitude overlaid (black contour = 10^{-2} , white contour = $10^{-1.8}$, and yellow contour = $10^{-1.2}$).

b. The ‘hot spot’ near 44° N, 180° E

The largest discrepancy between the model SSH amplitude and the coherence gain involves the large ‘hot spot’ in coherence gain that is centered near 44° N, 180° E. This is a remarkable feature both for the high value of the gain and for the degree of coherence with the TIWs - about half of the SSH variance in this region at 33-day periods can be predicted from the time series of SSH in the TIW region; roughly 6,000 km away. The model has a small local maximum in SSH amplitude at this point, but the relative amplitude is about $1/5^{\text{th}}$ the size of the observed gain, and numerous configuration adjustments failed to produce model SSH in this region with anything close to the amplitude seen in the observations. For instance, decreasing the friction coefficients did not produce a higher fraction of SSH amplitude at this location. Adjusting the forcing amplitude envelope to alter the initial wavenumber spectrum altered some of the SSH patterns at lower latitudes,

but we were not able to find a scenario that could produce the 44° N hotspot.

The SSH signal in the hot spot is strongly coherent with the TIWs, at a level high enough that it seems unlikely to be a coincidence (Fig. 4), but the barotropic model does not reproduce the hot spot. We can think of only two ways to simultaneously explain the existence of the hot spot, its coherence with the TIWs, and its absence in the model: either (1) the coherent variability in the hot spot is driven by the radiating waves but our model is somehow deficient, or (2) the coherent variability in the hot spot is driven by some mechanism other than radiating waves that happens to also be coherent with the TIW SSH signal (e.g., wind forcing).

The hot spot is centered near the termination of the model’s wave plume, in an apparent topographic cul-de-sac between the Aleutian Island chain to the north, the Emperor Seamount chain to the west, and a broad ridge to the south near 35° N, which extends from about 170° E

to 170° W. At first glance, it appears to be a natural configuration for producing a deep basin resonance similar to those described by Weijer et al. (2007) and Weijer (2008). To be sure that our grid spacing was not attenuating the boundaries of the cul-de-sac, the ridge line depths of the Emperor Seamounts and the 35° N ridge were extracted from the 1 minute bathymetry and inserted into the nearest grid points in our 1 degree bathymetry. (This is the bathymetry used to produce the model runs shown in Figs. 8 and 7). We also performed limited numerical experiments with 30 minute, and 20 minute grid spacing. None of these attempts produced a hot spot in the model SSH similar to that in the observed gain.

A feature that might argue against the deep basin resonance scenario is that there is a deep channel piercing the Emperor Seamount chain at about 40° N that shows up clearly in the 1 minute bathymetry. Combined with gaps between the Emperor Seamounts and the 35° N ridge, and between the northern end of the seamounts and the Aleutian Islands, this may be enough to make the otherwise shallow Emperor Seamount chain porous to barotropic Rossby waves (e.g. Pedlosky 2001). Still, the consistent location of the wave plume's termination suggests that a certain amount of wave energy is being trapped within the cul-de-sac, and we cannot rule out the possibility that model deficiencies are preventing the model from achieving a barotropic resonance that could be occurring in the real ocean near 44° N, 180° W.

Another possibility is that there is a forcing mechanism that is coherent with the TIW SSH signal but was not included in the model. Of the possible forcing mechanisms that could drive variability in the hot spot and be coherent with the TIW SSH signal, wind forcing seems the most likely. A considerable amount of previous work has implicated wind stress curl as a generally important mechanism for forcing barotropic Rossby waves (Muller and Frankignoul 1981; Niiler and Kobalinsky 1985; Niiler et al. 1993; Brink 1989; Samelson 1990; Fu 2003), and the hot spot is very close to the location where previous studies have identified wind-driven barotropic variability in intraseasonal period bands overlapping the frequencies of interest here (Luther et al. 1990; Chave et al. 1992; Fu 2003).

However, it is not clear why wind forced variability at this location would be coherent with the TIW signal. This could happen if the large-scale wind forcing sets the phase of the TIW variability (which is in fact believed to be the case, Benestad et al. 2001) and the same large-scale wind forcing also drives ocean SSH signals at higher latitudes. We cannot rule out the possibility that the high coherence at the hot spot could be mediated through the wind field, but this more complex causal chain seems less plausible to us than the idea that the coherence is a direct result of the radiating waves. It would be interesting to examine this situation in more realistic model experiments that include wind and pressure forcing.

Despite the fact that we do not understand the reason for the SSH signal seen at 44° N and around the Aleutian Islands that is coherent with the TIW SSH signal, the model results provide strong support for the conclusion that wave radiation is responsible for the coherent 33-day SSH signal seen stretching thousands of kilometers northward from the unstable equatorial current system.

c. Conclusion

In the introduction, we discussed the fact that the waves seemed to weaken dramatically and disappear near 20° N in the previous analysis by Farrar (2011). We posed the questions: What happens to these waves? Why do they disappear? We now have some insights into the answers to these questions.

On the question of what happens to the waves, we can conclude that the waves travel well north of 20° N. The data analysis here and the modeling study in the companion paper (Durland and Farrar submitted) both suggest that the waves travel to around 40° N with little decrease in SSH amplitude. The ultimate fate of the waves is not clear—the model shows the energy dissipating steadily as the waves move northward, but the observations show that the amplitude of the SSH signal coherent with the TIWs actually increases again near 45° N, 180° W. The reasons for this increase in amplitude remain a mystery, and there is a possibility that atmospheric forcing is a factor.

On the question of why the waves disappear by the time they reach 20° N, we have concluded that they do not in fact disappear. The better question is, “Why do the waves disappear near 20° N in the analysis of Farrar (2011)?” Two possible explanations mentioned in the introduction were that: (1) refraction of the waves by the topographic β -effect could cause the wavelength of the waves to change so much that the zonal wavelength is no longer within the passband of the filter that was used (10°–25° zonal wavelengths), and (2) that the waves might be distorted by the latitudinal variation in the filtering properties of the gridding algorithm used to produce DUACS gridded SSH product (Pujol et al. 2016). The first of those factors, alteration of the wavelength of the waves by refraction, is definitely relevant—Fig. 5 clearly shows that the zonal wavelength becomes longer as the waves move beyond 20° N.

However, the second of those factors, spatial variation of the temporal filtering in the DUACS gridded SSH product is apparently the dominant factor. The objective analysis method used to produce the DUACS product requires specification of autocovariance functions for the variability and for the measurement errors, which together set the filtering properties of the mapping algorithm. The values used in the autocovariance function for the DUACS mapping algorithm are not publicly available, but the zonally averaged temporal correlation scales

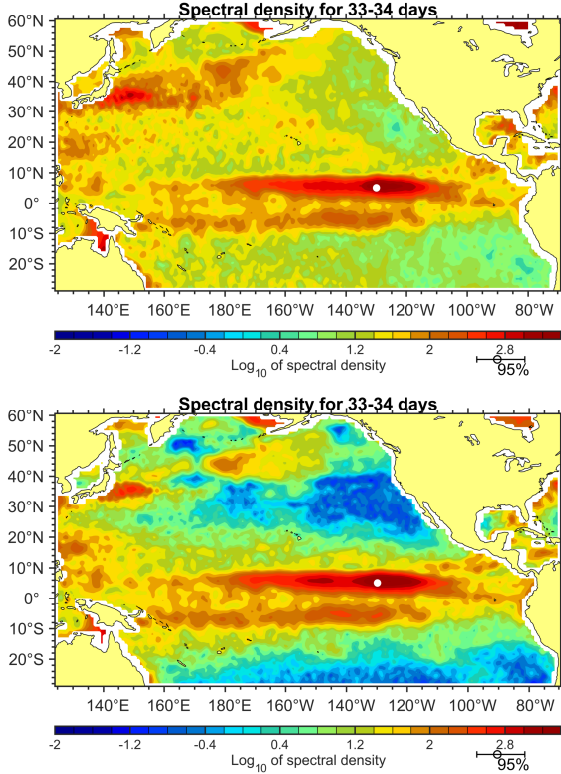


FIG. 9. Upper panel: Base-10 logarithm of spectral density of SSH (cm^2/cpd ; proportional to variance or squared amplitude) in the 33-day period band, computed from the gridded SSH product used here and described in Appendix A. This plot is identical to Fig. 3, but with an expanded dynamic range in the color scale. Lower panel: The same quantity computed using the DUACS2014 gridded SSH product (Pujol et al. 2016). In both panels, the 95% confidence interval for the spectrum is shown on the bottom-right side of the colorbar. The gridded SSH product used in the upper panel has spatially uniform temporal filtering, and we suspect that the difference in spatial patterns of 33-day variance is mostly due to spatial variations in temporal filtering in the DUACS product.

used in the autocovariance function reach a maximum in the $20\text{--}40^\circ\text{N}$ and $20\text{--}40^\circ\text{S}$ latitude bands (see Pujol et al. 2016, Fig. 4), which suggests that, on average, this is where high-frequency variability will be most strongly suppressed.

We performed an analysis identical to the one that led to the plots of 33-day spectral density, squared coherence amplitude, phase, and gain (Figs. 3–6), except that we used the DUACS2014 product (Appendix B). In the major regions of high 33-day variance (the tropical Pacific, the Kuroshio Extension, and the ‘hot spot’ in the North Pacific), the two SSH products are very similar—the 33-day spectral density of the two products agree within error bars, and the patterns of coherence amplitude and phase are similar. However, at the basin scale, the spatial patterns of 33-day variance are dramatically different in the

two products; in the $20\text{--}40^\circ\text{N}$ latitude band of the eastern Pacific that has been the focus here, the 33-day spectral density is roughly 100 times lower in the DUACS product (Fig. 9). The SSH maps used here and the DUACS product were constructed from the same along-track data, with the same corrections. The only difference is that the gridded SSH product used here was deliberately constructed to have spatially uniform temporal filtering, so we are led to conclude that the spatial pattern of 33-day variance in the DUACS product must be dominated by the assumed form of the autocovariance function used for the objective mapping scheme.

Acknowledgments. The along-track altimetry data used in this study are produced and distributed by the Copernicus Marine and Environment Monitoring Service (CMEMS) (<http://www.marine.copernicus.eu>). This work was supported by NASA grants NNX13AE46G, NNX14AM71G, and NNX17AH54G. We are grateful the helpful comments and criticism provided by two anonymous reviewers. We thank Dudley Chelton, Gerald Dibarbouré, Joe Pedlosky, Ryan Holmes, Rick Lumpkin, Shafer Smith, Cesar Rocha, and Navid Constantinou for helpful discussions.

APPENDIX A

Gridding of along-track altimetry data

Although there is a readily available and widely-used global gridded data product, often referred to as the DUACS product (Le Traon et al. 1998; Ducet et al. 2000; Le Traon et al. 2003; Pujol et al. 2016), this product has considerable spatial structure in its space/time smoothing properties that attenuates 30-day variability in the midlatitudes. We thus found it desirable to create a mapped product with uniform spatial and temporal smoothing. We did this using the following procedure:

1. We averaged the altimetry data along-track in 0.25° latitude bins.
2. We mapped the data to a uniform space-time grid ($0.5^\circ \times 0.5^\circ \times 3$ days) using a Gaussian smoother (weighted average) having nominal half-power points of $6^\circ \times 6^\circ \times 17$ days. Specifically, the SSH (h_n) at each grid point was estimated as a weighted average of the measured SSH (g_m) at the nearby points as follows:

$$h_n = \frac{\sum_{m=1}^M e^{-2(ar)^2} g_m}{\sum_{m=1}^M e^{-2(ar)^2}} \quad (\text{A1})$$

with

$$r^2 = \frac{x^2}{L_x^2} + \frac{y^2}{L_y^2} + \frac{t^2}{L_t^2} \quad (\text{A2})$$

and

$$L_{x,y,t} = \frac{0.775}{\omega_{\text{cutoff}}} \quad (\text{A3})$$

where x , y , and t are the longitude, latitude, and time distances from the grid point, $a=3$ and ω_{cutoff} is the nominal half-power frequency of the gridding kernel in a given dimension (latitude, longitude, or time). The summation is carried out using all of the M along-track measurements that are within the scaled distance $|r| < 1/2$ of the grid point being estimated. The properties of this Gaussian smoothing window and its associated filter transfer function are discussed, for example, by Harris (1978) and Schlax and Chelton (1992).

3. If the number of SSH observations within $|r| < 1/2$ of the grid point being estimated was less than 6 (i.e., $M \leq 5$ in A1), no estimate was made. This happens only rarely and appears to be associated with brief satellite data outages during times when there were only two operating altimeters (e.g., around December 1995). When these gaps occur, they are of limited zonal extent, and the gaps are filled by linear interpolation in longitude.

APPENDIX B

Barotropic wave signal in the DUACS gridded product

The DUACS gridded data product uses the same along-track altimetry data that we use here, but it is produced by using a Gauss-Markov (or “optimal interpolation”) estimate that is supposed to take account of prior information about the autocovariance of the measurement noise and the underlying physical signal. The filtering properties of the Gauss-Markov estimate will depend on: (1) the assumed SSH and error covariance functions, (2) the assumed signal-to-noise ratio, and (3) the time-space sampling.

The assumed error covariance includes a contribution from uncorrelated random errors and from errors that are correlated along the satellite track to account for so-called long-wavelength orbit and geophysical correction errors (Pujol et al. 2016). This “long-wavelength error” (LWE) correction provides a means of identifying and removing signals that are correlated along the satellite tracks but not between different tracks and is an effective strategy (Le Traon et al. 1998) for removing errors in the estimated orbit and errors in atmospheric corrections (e.g., wet tropospheric delay). The LWE correction is especially important for the missions that have less precisely known spacecraft altitudes and orbits (like *ERS-1*). The LWE correction also would tend to remove any real oceanic variability

that has large scales along satellite tracks and that is incoherent from one track to another (e.g., because the cross-track length scale or the time scale is shorter than the separation between successive tracks). The DUACS along-track data product that we used to produce the gridded data set described in Appendix c includes the LWE correction, so, while the LWE correction may remove some of the barotropic signal of interest, it does not explain any difference between our gridded product and the DUACS product.

The assumed SSH covariance function involves temporal and spatial decorrelation scales and a propagation speed and direction that vary as a function of latitude and longitude (Pujol et al. 2016). The actual values of the temporal and spatial decorrelation scales used in the DUACS product are not publicly available, but Pujol et al. (2016) show the zonally averaged value of the decorrelation time scale and zonal length scale (their Figure 4). Between the equator and 20°N, the zonally averaged decorrelation time scale triples (from about 10 days to about 30 days). This could have a profound effect on the spatial variations of 30-day variance in the DUACS product; in fact, we believe the assumed decorrelation time scale is the dominant factor setting the spatial variations of 30-day variance.

To investigate this possibility, we performed an analysis identical to the one that led to the plots of 33-day spectral density, squared coherence amplitude, phase, and gain (Figs. 3-6) using the DUACS2014 product. In order to have an amount of spatial smoothing similar to that in the gridded SSH product that we made, we filtered the DUACS2014 product with a Gaussian weighted average smoother that had half-amplitude wavelengths of 2° in latitude and longitude (meaning that the amplitude of the variability is reduced by 1/2 for wavelengths of 2°, with stronger filtering at shorter wavelengths). We then subsampled the DUACS data product to the 0.5° × 0.5° latitude-longitude grid used for our gridded product and performed exactly the same calculations (with the same code) used to generate Figs. 3-6.

Comparison of the 33-day variance in the DUACS2014 product to that in the gridded SSH product described in Appendix A (Fig. 9) shows quantitatively close agreement in some of the major areas of 33-day variance. This is perhaps most obvious in the tropical Pacific, where there is close agreement in both the patterns and the absolute level of 33-day variance; the two estimates are essentially indistinguishable (within 95% confidence intervals) within 10°S-10°N. In this region, the DUACS mapping procedure uses a short correlation timescale in the autocovariance function (Pujol et al. 2016). Despite these quantitative similarities in the tropical Pacific, the overall patterns of the 33-day variance maps look completely different, with differences exceeding a factor of 100 in many places and over vast regions (especially in the 20-40°N region). (A

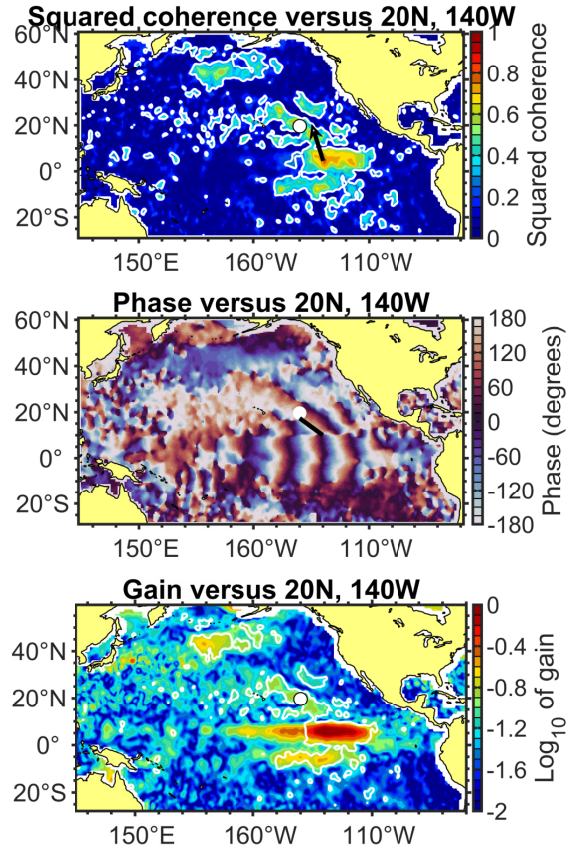
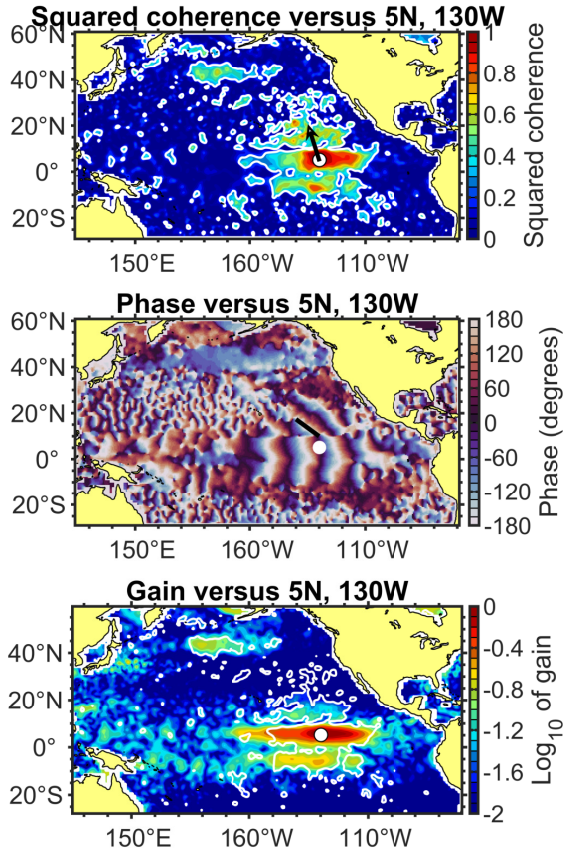


FIG. B10. Squared coherence amplitude (upper panel), phase (middle panel), and gain (lower panel) versus 5°N, 130°W in the DUACS2014 gridded SSH product (Pujol et al. 2016). These figures should be compared with Figs. 4-6.

FIG. C11. Squared coherence amplitude (upper panel), phase (middle panel), and gain (lower panel) computed using a different reference location (20°N, 140°W, indicated by a white dot in each panel). To aid comparison with Figs. 5 and 6, the gain has been renormalized to equal one at 5°N, 130°W, and a uniform offset has been applied to the phase so that it is equal to 0° at 5°N, 130°W. These figures should be compared to Fig. C12 and Figs. 4-6.

factor of 100 is more than 25 times larger than the 95% confidence interval.)

Despite the large difference in the spatial pattern of 33-day variance, the spatial patterns of squared coherence amplitude and phase are quite similar in the DUACS gridded product and the one analyzed here (compare Fig. B10 to Figs. 4-6). Given that our SSH product was deliberately constructed to have spatially uniform temporal filtering, it seems like spatial variations in the temporal filtering in the DUACS product provide the most obvious way to rationalize the large difference in 33-day variance and the similarity in phase and coherence. This observation is not meant to be a criticism of the DUACS product, because the timescales for the autocovariance function have been carefully optimized for representation of mesoscale eddies. For most purposes, the DUACS product probably provides a better estimate of SSH variability, but it is not appropriate for tracking the propagation of ~30-day waves over thousands of kilometers.

APPENDIX C

Sensitivity to choice of reference location

For the analysis in the main text, the reference location for the cross-spectral calculations was chosen as the place where the TIW SSH signal is strongest (5°N, 130°W, which we will refer to here as the “primary reference location”). In this appendix, we present representative results obtained using other choices for the reference location.

The gross patterns of squared coherence amplitude, coherence phase, and gain are very similar to those seen in the main text when using reference locations where the SSH signal is coherent with that at the primary reference location. For example, Figs. C11 and C12 show the squared coherence amplitude, coherence phase, and gain maps computed using 20°N, 140°W and 43°N, 175°W as reference locations. To facilitate comparison with Figs. 5

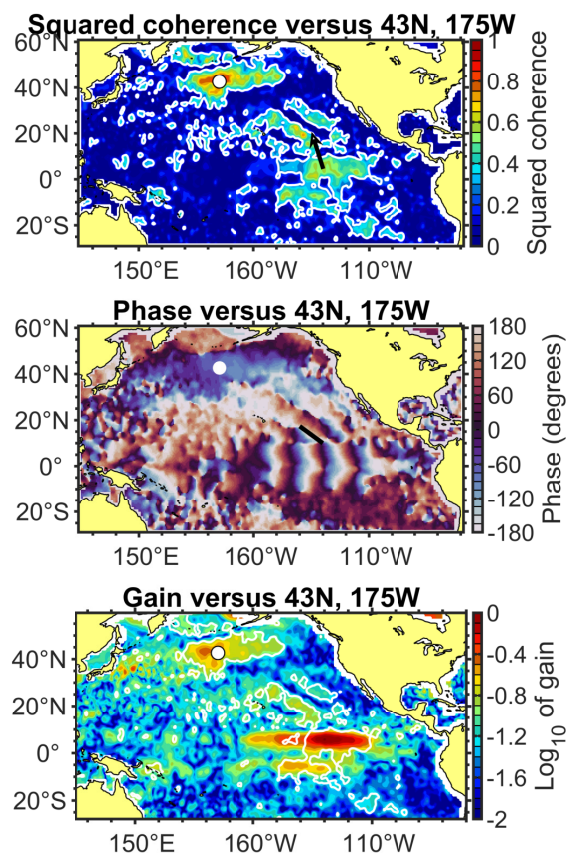


FIG. C12. Squared coherence amplitude (upper panel), phase (middle panel), and gain (lower panel) computed using a different reference location (43°N , 175°W , indicated by a white dot in each panel). To aid comparison with Figures 5 and 6, the gain has been renormalized to equal one at 5°N , 130°W , and a uniform offset has been applied to the phase so that it is equal to 0° at 5°N , 130°W . These figures should be compared to Fig. C11 and Figs. 4-6.

and 6, we rescaled the gain to have a value of one at the primary reference location, and we applied a uniform phase offset so that the phase has a value of 0° at the primary reference location.

These alternate reference locations are places where the SSH signal is coherent with that at the primary reference location (Fig. 4), but it is not a trivial result that the spatial patterns of the cross-spectral quantities should be almost the same regardless of whether the reference location is where the TIW SSH signal is strongest (5°N , 130°W) or at 20°N , 140°W or 43°N , 175°W . For example, the variability at 20°N , 140°W could be incoherent with that at 43°N , 175°W , even if they are both coherent with 5°N , 130°W . The similarity of the patterns that result when using different reference locations provides further support to the idea that there is a mutually coherent pattern of variability, which was an underlying assumption of our interpretation of the coherence, gain, and phase patterns.

In fact, the results depicted in Fig. C12 tell us something quite remarkable: the SSH signal in the northern ‘hot spot’ near 43°N , 175°W is so closely related to the SSH variability in the tropical Pacific that one can explain about half of the SSH variance in the TIW region at 33-day periods and reproduce the pattern of amplitude and phase with surprising detail (compare lower two panels of Fig. C12 to Figs. 5 and 6).

References

- AVISO/CLS, 2015: SSALTO/DUACS User Handbook: (M)SLA and (M)ADT Near-Real Time and Delayed Time Products. Tech. rep., AVISO/CLS: CLS-DOS-NT-06-034, Issue 4.4, Date: 2015/06/30, Toulouse, France. Available at http://www.aviso.altimetry.fr/fileadmin/documents/data/tools/hdbk_duacs.pdf.
- Bendat, J. S., and A. G. Piersol, 2010: *Random Data: Analysis and Measurement Procedures (Fourth Edition)*. Wiley-Interscience, New York.
- Benestad, R., R. Sutton, M. Allen, and D. Anderson, 2001: The influence of subseasonal wind variability on tropical instability waves in the Pacific. *Geophys. Res. Lett.*, **28**, 2041–2044.
- Bloomfield, P., 2000: *Fourier Analysis of Time Series: An Introduction (Second Edition)*. John Wiley & Sons, Inc., New York, NY.
- Bower, A. S., and N. G. Hogg, 1992: Evidence for barotropic wave radiation from the Gulf Stream. *J. Phys. Oceanogr.*, **22**, 42–61.
- Brink, K. H., 1989: Evidence for wind-driven current fluctuations in the western North Atlantic. *J. Geophys. Res.*, **94**, 2029–2044.
- Brink, K. H., and J. Pedlosky, 2020: The structure of baroclinic modes in the presence of baroclinic mean flow. *Journal of Physical Oceanography*, **50**, 239–253, doi:10.1175/JPO-D-19-0123.1.
- Chave, A. D., D. S. Luther, and J. H. Filloux, 1992: The Barotropic Electromagnetic and Pressure Experiment 1. Barotropic response to atmospheric forcing. *J. Geophys. Res.*, **97**, 9565–9593.
- Chelton, D. B., and M. G. Schlax, 1994: The resolution capability of an irregularly sampled dataset: With application to Geosat altimeter data. *J. Atmos. Ocean. Tech.*, **11**, 534–550.
- Cox, M. D., 1980: Generation and propagation of 30-day waves in a numerical model of the Pacific. *J. Phys. Oceanogr.*, **10**, 1168–1186.
- Ducet, N., P. Y. Le Traon, and G. Reverdin, 2000: Global high-resolution mapping of ocean circulation from TOPEX/Poseidon and ERS-1 and -2. *J. Geophys. Res.*, **105**, 19,477–19,498.
- Durland, T. S., and J. T. Farrar, 2020: Another note on Rossby wave energy flux. *Journal of Physical Oceanography*, **50**, 531–534.
- Durland, T. S., and J. T. Farrar, submitted: Model of 33-day barotropic Rossby waves in the North Pacific. *Journal of Physical Oceanography*.
- Farrar, J. T., 2008: Observations of the dispersion characteristics and meridional sea level structure of equatorial waves in the Pacific Ocean. *J. Phys. Oceanogr.*, **38**, 1669–1689.
- Farrar, J. T., 2011: Barotropic Rossby waves radiating from tropical instability waves in the Pacific Ocean. *J. Phys. Oceanogr.*, **41**, 1160–1181.

- Fu, L.-L., 2003: Wind-forced intraseasonal sea level variability of the extratropical oceans. *J. Phys. Oceanogr.*, **33**, 436–449.
- Harris, F., 1978: On the use of windows for harmonic analysis with the discrete Fourier transform. *Proceedings of the IEEE*, **66**, 51–83.
- Hogg, N. G., 1988: Stochastic wave radiation by the Gulf Stream. *J. Phys. Oceanogr.*, **18**, 1687–1701.
- Holmes, R. M., and L. N. Thomas, 2016: Modulation of tropical instability wave intensity by equatorial Kelvin waves. *J. Phys. Oceanogr.*, **46**, 2623–2643, doi:10.1175/JPO-D-16-0064.1.
- Jayne, S., N. Hogg, and P. Malonotte-Rizzoli, 1996: Recirculation gyres forced by a beta-plane jet. *J. Phys. Oceanogr.*, **26**, 492–504.
- Le Traon, P. Y., Y. Faugère, F. Hernandez, J. Dorandeu, F. Mertz, and M. Ablain, 2003: Can we merge *GEOSAT Follow-On* with TOPEX/Poseidon and *ERS-2* for an improved description of the ocean circulation? *J. Atmos. Oceanic Technol.*, **20**, 889–895.
- Le Traon, P. Y., F. Nadal, and N. Ducet, 1998: An improved mapping method of multisatellite altimeter data. *J. Atmos. Oceanic Technol.*, **15**, 522–534.
- Lee, T., J. Farrar, S. Arnault, D. Meyssignac, W. Han, and T. Durland, 2018: Monitoring and interpreting the tropical oceans by satellite altimetry. *Satellite Altimetry Over Ocean and Land Surfaces*, D. Stammer, and A. Cazenave, Eds., CRC Press, Taylor and Francis Group, New York, NY, 231–270.
- Longuet-Higgins, M., 1965: Planetary waves on a rotating sphere. II. *Proc. Roy. Soc. London*, **284**, 40–68.
- Luther, D. S., A. D. Chave, J. H. Filloux, and P. F. Spain, 1990: Evidence for local and nonlocal barotropic responses to atmospheric forcing during BEMPEX. *Geophys. Res. Lett.*, **17**, 949–952.
- Lyman, J. M., D. B. Chelton, R. A. deSzoeke, and R. M. Samelson, 2005: Tropical instability waves as a resonance between equatorial Rossby waves. *J. Phys. Oceanogr.*, **35**, 232–254.
- McIntyre, M. E., and M. A. Weissman, 1978: On radiating instabilities and resonant overreflection. *J. Atmos. Sci.*, **35**, 1190–1196, doi:10.1175/1520-0469(1978)035<1190:ORARIO>2.0.CO;2.
- Miller, A. J., and Coauthors, 2007: Barotropic rossby wave radiation from a model Gulf Stream. *Geophys. Res. Lett.*, **34**, doi:10.1029/2007GL031937.
- Mizuta, G., 2009: Rossby wave radiation from an eastward jet and its recirculations. *J. Mar. Res.*, **67**, 185–212.
- Muller, P., and C. Frankignoul, 1981: Direct atmospheric forcing of geostrophic eddies. *J. Phys. Oceanogr.*, **11**, 287–308.
- Niiler, P. P., J. Filloux, W. T. Liu, R. M. Samelson, J. D. Paduan, and C. A. Paulson, 1993: Wind-forced variability of the deep eastern North Pacific: Observations of seafloor pressure and abyssal currents. *J. Geophys. Res.*, **98**, 22,589–22,602.
- Niiler, P. P., and C. Koblinsky, 1985: A local time-dependent Sverdrup balance in the eastern north Pacific Ocean. *Science*, **229**, 754–756.
- Pedlosky, J., 2001: The transparency of ocean barriers to Rossby waves: The Rossby slit problem. *J. Phys. Oceanogr.*, **31**, 336–352.
- Pujol, M.-I., Y. Faugère, G. Taburet, S. Dupuy, C. Pelloquin, M. Ablain, and N. Picot, 2016: DUACS DT2014: The new multi-mission altimeter data set reprocessed over 20 years. *Ocean Sci.*, **12**, 1067–1090, doi:10.5194/os-12-1067-2016.
- Rhines, P., 1970: Edge-, bottom-, and Rossby waves in a rotating stratified fluid. *Geophys. Fluid Dynam.*, **1**, 273–302.
- Samelson, R. M., 1990: Evidence for wind-driven current fluctuations in the eastern North Atlantic. *J. Geophys. Res.*, **95**, 11,359–11,368.
- Schlax, M. G., and D. B. Chelton, 1992: Frequency domain diagnostics for linear smoothers. *J. Amer. Stat. Assoc.*, **87**, 1070–1081.
- Schlax, M. G., D. B. Chelton, and M. H. Freilich, 2001: Sampling errors in wind fields constructed from single and tandem scatterometer datasets. *J. Atmos. Oceanic Technol.*, **18**, 1014–1036.
- Song, Y. T., and V. Zlotnicki, 2004: Ocean bottom pressure waves predicted in the tropical Pacific. *Geophys. Res. Lett.*, **31** (L05306), doi:10.1029/2003GL018980.
- Spall, M. A., 1992: Rossby wave radiation in the Cape Verde frontal zone. *J. Phys. Oceanogr.*, **22**, 796–807.
- Sutherland, B. R., C. P. Caulfield, and W. R. Peltier, 1988: Internal gravity wave generation and hydrodynamic instability. *J. Atmos. Sci.*, **51**, 3261–3280.
- Talley, L. D., 1983b: Radiating instabilities of thin baroclinic jets. *J. Phys. Oceanogr.*, **13**, 2161–2181.
- Thompson, R. O. R. Y., 1979: Coherence significance levels. *J. Atmos. Sci.*, **36**, 2020–2021.
- Waterman, S., N. G. Hogg, and S. R. Jayne, 2011: Eddy-mean flow interaction in the kuroshio extension region. *J. Phys. Oceanogr.*, **41**, 1182–1208, doi:10.1175/2010JPO4564.1.
- Waterman, S., and S. R. Jayne, 2011: Eddy-mean flow interactions in the along-stream development of a western boundary current jet: An idealized model study. *J. Phys. Oceanogr.*, **41**, 682–707, doi:10.1175/2010JPO4477.1.
- Weijer, W., 2008: Normal modes of the Mascarene Basin. *Deep Sea Res. I*, **55**, 128–136.
- Weijer, W., F. Vivier, S. T. Gille, and H. A. Dijkstra, 2007: Multiple oscillatory modes of the Argentine Basin. Part I: Statistical analysis. *J. Phys. Oceanogr.*, **37**, 2855–2868.
- Wunsch, C., 1989: Sampling characteristics of satellite orbits. *J. Atmos. Ocean. Tech.*, **6**, 891–907.